Linking entropy at rest with the underlying structural connectivity in the healthy and lesioned brain

Victor M. Saenger, Adrián Ponce-Alvarez, Mohit Adhikari, Patric Hagmann, Gustavo Deco & Maurizio Corbetta.

Supplementary Material

Methods

Scanning for functional data

Functional scans of all subjects and healthy participants were collected with a Siemens 3T Tim-Trio scanner at the School of Medicine in Washington University, St. Louis. Patients underwent a scanning session within 2 weeks after suffering a stroke. Structural scanning consisted of (1) a sagittal MPRAGE T1-weighted image with TR of 1950 ms, an TE of 2.26 ms and a flip angle of 90° with voxel size = 1.0mm^3 and slice thickness = 1.00 mm. (2) A transverse turbo spin-echo T2-weighted image (TR= 2500 ms, TE = 435 ms, voxel-size = 1.0mm^3 and slice thickness = 1.00 mm). (3) A sagittal FLAIR (TR= 7500 ms, TE= 326 ms, voxel-size = 1.5mm^3, slice thickness = 1.50 mm). PASL acquisition parameters were: TR = 2600 ms, TE = 13 ms, flip angle = 90°, bandwidth 2.232 kHz/pixel, and field of view of 220 mm. A total of 120 volumes were acquired (322 s total), all containing 15 slices with a slice thickness of 6- and a 23.7-mm gap. Resting state functional scans were acquired with a gradient echo EPI sequence (TR = 2000 ms, TE = 27 ms, 32 contiguous 4-mm slices and a 4 × 4 mm in-plane resolution) during which participants were instructed to fixate on a small cross in a low luminance setting. A total of 30 minutes of resting activity was acquired after six to eight runs including 128 volumes each.

Preprocessing and quality control

Preprocessing was performed in the following manner. First, asynchronous slice acquisition was compensated by sinc interpolation; followed by elimination of odd/even slice intensity differences resulting from interleaved acquisition. Then whole-brain

normalization was performed to correct for changes in signal intensity across scans and data were realigned within/across scans to correct for head movement. EPI data was co-registered to each subject-specific T2-weighted image, which in turn was co-registered with the T1-weighted MPRAGE (Rowland *et al.*, 2005). The MPRAGE was then transformed to the Talairach and Tournoux atlas space using a 12-parameter affine transformation. Movement correction and atlas transformation was done in one resampling step (resulting in an isotropic 3 mm voxel size) to minimize motion blur.

Data for functional MRI analysis was preprocessed following a number steps including spatial smoothing (6 mm full-width at half-maximum Gaussian blur), temporal filtering retaining within the 0.009–0.08 Hz band and removal of spurious noisy sources through linear regression including six parameters obtained by rigid body correction of head motion, whole-brain signal averaged over a fixed region in atlas space (Satterthwaite et al. 2012; Power et al. 2015), signals arising from a ventricular region of interest; as well as signals from a region centered in the white matter. Resting state data was finally quality-controlled by using temporal derivative of time courses of root mean square variance over voxels (Power et al. 2012).

Large-scale dynamic modeling of brain activity

All simulated functional connectivity matrices were computed by using a dynamic mean-field model that takes into account the structural connectivity as a blueprint for global coupling. The model has N regions, each composed of an arrangement of excitatory – inhibitory subnetworks. Each brain region is composed of excitatory–inhibitory subnetworks (E–I networks). The dynamics of each of the E-I nodes follows the mean field equations derived by (Wong and Wang 2006) and the excitatory firing rate is clamped around 3 Hz by adjusting the connection weight from the I population to the E population, a procedure known as Feedback Inhibition Control (FIC) (Deco et al. 2014). This large-scale model has been shown to provide an efficient description of resting-state fMRI functional connectivity together with realistic stimulus-evoked activity. The stochastic differential equations of the model describe the time evolution of the mean synaptic activity of each local node (i.e., brain region) and there are given by:

$$u_i^{(\mathrm{E})} = I_{0,E} + w_{EE} S_i^{(E)} + G \sum_j C_{ij} S_j^{(E)} - w_{EI,i} S_i^{(I)}, \quad (1)$$

$$u_i^{(\mathrm{I})} = I_{0,I} + w_{IE} S_i^{(E)} - w_{II} S_i^{(I)}, \quad (2)$$

$$r_i^{(E)} = \Phi_E(u_i^{(E)}) = \frac{a_E u_i^{(E)} - b_E}{1 - \exp(-d_E(a_E u_i^{(E)} - b_E))}, \quad (3)$$

$$r_i^{(I)} = \Phi_I(u_i^{(I)}) = \frac{a_I u_i^{(I)} - b_I}{1 - \exp(-d_I(a_I u_i^{(I)} - b_I))}, \quad (4)$$

$$\frac{dS_i^{(E)}}{dt} = -\frac{S_i^{(E)}}{\tau_E} + (1 - S_i^{(E)})\gamma r_i^{(E)} + \beta \eta_i^{(E)}(t), \quad (5)$$

$$\frac{dS_i^{(I)}}{dt} = -\frac{S_i^{(I)}}{\tau_I} + r_i^{(I)} + \beta \eta_i^{(I)}(t), \quad (6)$$

where $S_i^{E,I}$ denotes the average excitatory or inhibitory synaptic gating variable (i.e., fraction of open channels) at the local area *i* ($i \in [1,...,N]$). In equations 5 and 6 $\eta_i^{(E)}(t)$ and $\eta_i^{(I)}(t)$ are uncorrelated Gaussian noises and the noise amplitude at each node is β=0.01. $r_i^{E,I}$ denotes the population firing rate of the excitatory (E) or inhibitory (I) population in the brain area *i*, and is a sigmoid function (Φ_I and Φ_E) of the input synaptic currents to the excitatory or inhibitory population ($u_i^{E,I}$). The local currents in node *i* are the sum of constants inputs to excitatory and inhibitory populations, noted $I_{0,E}$ and $I_{0,I}$, respectively, local excitatory-to-excitatory currents $w_{EE} S_i^{(E)}$, local inhibitory-to-excitatory currents $w_{EI,i} S_i^{(I)}$, local excitatory-to-inhibitory currents $w_{IE} S_i^{(E)}$, and local inhibitory-to-inhibitory currents $w_{II} S_i^{(I)}$. The weights of these local connections are given by: $w_{EE} = 0.21$; $w_{IE} = 0.15$; $w_{II} = 1$; and the feedback inhibition weight, $w_{EI,i}$, is adjusted for each node *i* so that the firing rate of the local excitatory neural population is clamped around 3Hz, whenever nodes are connected or not — this regulation is known as Feedback Inhibition Control (FIC) and the algorithm to achieve it is described in Deco et al. (2014). It has been shown that the FIC constrain leads to a better prediction of the resting functional connectivity and a more realistic network evoked activity (Deco et al. 2013; Deco et al. 2014). Local E–I networks interact through excitatory connections given by the *N*-by-*N* anatomical connectivity matrix, noted **C**.

The connectivity matrix was scaled by a single global parameter, *G*, that changed the network from weakly to strongly connected and determined the dynamical state of the system. As shown in Deco et al. (2014) the model has one single stable fixed point of low firing activity in all cortical areas, for all values of *G* within the region where the FIC regulation can be achieved. For larger values of G, long-range interactions are too strong to be compensated by FIC and the activity diverges. Finally, the modeled synaptic activity was transformed to BOLD signals using the Balloon-Windkessel hemodynamic model (Friston et al. 2003), allowing the construction of a simulated functional connectivity matrix.

Fitting of stroke patients

An important aspect of the current study was the construction of modeled stroke FC matrices base on artificially-lesioned backbones. The same procedure applied to the healthy modeled data was applied to each of the subjects. In short, based on the lesioned node information from each subject, the average healthy SC was "lesioned" 18 independent times (one per subject) creating 18 artificially-lesioned networks. These networks were used to model stroke FCs, which were finally fitted to the empirical stroke FCs (Fig 1) to find all optimal modeled FCs. This means that each subject has its own fitting curve (Fig S1). Note that the mean stroke fitting is lower than the mean healthy fitting, which is consistent with previous findings (Adhikari et al. 2015)

Finer parcellation cohort

As a quality control analysis, we used a supplementary set of 29 Healthy and 29 stroke patients from the same original cohort (Corbetta et al. 2015) to understand the impact of using a finer parcellation. For this, BOLD signals following the same acquisition and preprocessing procedures described above were extracted from a set of 114 nodes from the Desikan-Killiany scheme (Desikan et al. 2006) to further reconstruct subject-specific FC matrices. These matrices were then used to explore the impact that lesion severity has on node entropy using the same procedure described in the main text after filtering a total of 314 affected nodes. Lesioned node location indexes were used to filter entropy values from healthy controls. Additionally, we investigated the impact that stroke has on homotopic connectivity and on global diffusion of information using the random walker algorithm.

Random walker algorithm

It is of great interest to clarify if a higher diversity of functional weights leads to easier communication efficiency. Inspired by the work done by Rosvall and Bergstrom (Rosvall and Bergstrom 2007; Rosvall and Bergstrom 2008), we created a semi-random walker algorithm and measure its ability to diffuse through the network. First, a walker was set at a random initial node in the network and diffused to a neighboring node based on a probabilistic approach such that it diffused through links with higher weights more frequently. To do this, the original functional weights of each of the nodes in a given network matrix M need to be transformed in such a way that weights corresponds to out-probabilities of the random walker and the sum of all probabilities on every node is always 1. For a given weight in a node *i*, this probability is simply given by:

$$p(w_{ij}) = \frac{w_{ij}}{\sum_{j=1}^{n} w_{ij}} \qquad (7)$$

where w_{ij} is the weight *j* of node *i* and *n* is the total amount of nodes in the network. The probability matrix *p*(M) is then constructed:

$$p(\mathrm{M}) = \begin{bmatrix} p(w_{ij}) & \cdots & p(w_{in}) \\ \vdots & \ddots & \vdots \\ p(w_{nj}) & \cdots & p(w_{nn}) \end{bmatrix} \qquad (8)$$

We then let the walker explore or diffuse over *p*(M) without imposing restrictions in directionality until it visited all nodes in the network at least one time. When it reached 250 steps, we measured the network visit percentage, that is, the percentage of different nodes out of the total the walker visited. This simulation was repeated 1000 times and a mean network visit percentage was then computed. To avoid trapped walkers (inside a highly connected clusters), we added a fixed random teleportation probability (Brin and Page 1998) of 0.1.

In order to explore if the intrinsic distribution of functional weights maximizes walker diffusion, the out-probabilities in each node of *p*(M) were progressively shifted either by adding randomness or predictability to the walker out-probability. To add randomness, the weights were gradually changed such that the probability of a walker to choose its next node becomes as random as possible (Fig. S5*A*). To make it more predictable (rigid), the

most prominent weight became increasingly more prominent such that the walker diffuses through it with much higher probability compared to the original unshifted network (Fig. S5*A*). Note that in p(M) terms, adding randomness means having increasingly equal out-probabilities and hence less diffusion predictability. Finally, we let the walker diffuse over the network in each of these weight-shifted networks and the mean network visit percentage was computed over 1000 simulations per weight-shifted network as previously described. This allowed evaluating the consequence of varying functional weight diversity in terms of network communication.

Results

Diffusion of Information

The semi-random walker procedure suggested that the original network presented a weight distribution that maximizes the efficiency of information flow, creating a trade-off between predictability and randomness. Figure S5*B-C* shows the network visit percentage for the original and weight-shifted networks. At 250 steps the walker diffused over 94% of all nodes in the original configuration (Fig. S5*B*). An almost random connection weight diversity slightly increased this percentage to 97%, while high weight predictability (biased out-probability) drastically deteriorated the efficiency of the walker from 94% to 36% (Fig. S5*B*). The surface plot (color map) in Figure S5*C* represents a network visit percentage landscape with gradual weight shifting (see supplementary methods) further clarifying the idea of an optimal working point in the original FC with unshifted weight distributions.

Effect of stroke in entropy using a finer parcellation

Lesion severity had a negative impact on entropy in stroke patients (r = -0.15, p = 0.007) but not in healthy controls (r = 0.04, p = 0.47) corroborating our main findings. In addition, similar to what we found with the original data set, lesion severity negatively correlated with homotopic connectivity (r = -0.18, p = 0.001) while node entropy showed a positive correlation (r = 0.40, p < 0.0001). Globally, homotopic connectivity of stroke patients (0.32 ± 0.23) was significantly lower than that of healthy controls (0.51 ± 0.26), which again supports the uncovered impact of lesions on aspects of functional connectivity. Finally, diffusion of information was also significantly

affected in strokes compared with controls evidenced by a significantly larger diffusion time. Taken together these results indicated that using a finer parcellation yielded very similar results and can be found in Figure S3.

References

Adhikari MH, Raja Beharelle A, Griffa A, Hagmann P, Solodkin A, McIntosh AR, Small SL, Deco G. 2015. Computational modeling of resting-state activity demonstrates markers of normalcy in children with prenatal or perinatal stroke. J Neurosci. 35:8914-8924.

Brin S, Page L. 1998. The Anatomy of a Search Engine. Search.1-9.

Corbetta M, Ramsey L, Callejas A, Baldassarre A, Hacker CD, Siegel JS, Astafiev SV, Rengachary J, Zinn K, Lang CE, Connor LT, Fucetola R, Strube M, Carter AR, Shulman GL. 2015. Common behavioral clusters and subcortical anatomy in stroke. Neuron. 85:927-941.

Deco G, Ponce-Alvarez A, Hagmann P, Romani GL, Mantini D, Corbetta M. 2014. How local excitation-inhibition ratio impacts the whole brain dynamics. J Neurosci. 34:7886-7898.

Deco G, Ponce-Alvarez A, Mantini D, Romani GL, Hagmann P, Corbetta M. 2013. Resting-state functional connectivity emerges from structurally and dynamically shaped slow linear fluctuations. The Journal of neuroscience : the official journal of the Society for Neuroscience. 33:11239-11252.

Desikan RS, Segonne F, Fischl B, Quinn BT, Dickerson BC, Blacker D, Buckner RL, Dale AM, Maguire RP, Hyman BT, Albert MS, Killiany RJ. 2006. An automated labeling system for subdividing the human cerebral cortex on MRI scans into gyral based regions of interest. NeuroImage. 31:968-980.

Friston KJ, Harrison L, Penny W. 2003. Dynamic causal modelling. NeuroImage. 19:1273-1302.

Power JD, Barnes KA, Snyder AZ, Schlaggar BL, Petersen SE. 2012. Spurious but systematic correlations in functional connectivity MRI networks arise from subject motion. NeuroImage. 59:2142-2154.

Power JD, Schlaggar BL, Petersen SE. 2015. Recent progress and outstanding issues in motion correction in resting state fMRI. NeuroImage. 105:536-551.

Rosvall M, Bergstrom CT. 2007. An information-theoretic framework for resolving community structure in complex networks Martin Rosvall, and Carl T. Bergstrom. PNAS. 104:7327.

Rosvall M, Bergstrom CT. 2008. Maps of random walks on complex networks reveal community structure. Proc Natl Acad Sci U S A. 105:1118-1123.

Satterthwaite TD, Wolf DH, Loughead J, Ruparel K, Elliott MA, Hakonarson H, Gur RC, Gur RE. 2012. Impact of in-scanner head motion on multiple measures of functional connectivity: relevance for studies of neurodevelopment in youth. NeuroImage. 60:623-632.

Wong KF, Wang XJ. 2006. A recurrent network mechanism of time integration in perceptual decisions. J Neurosci. 26:1314-1328.

Tables and figure legends

Excitatory gating variables
a_E = 310 (nC^{-1})
b_E =125 (Hz)
d_E=0.16 (s)
$\tau_E = \tau_{NMDA}$=100 (ms)
$I_{0,E}$=0.3820 (nA)
Inhibitory gating variables
a_I = 615 (nC^{-1})
b_I =177 (Hz)
d_I =0.087 (s)
$\tau_I = \tau_{GABA}$= 10 (ms)
$I_{0,I}$ =0.2674 (nA)
Local connectivity parameters
$w_{E\,E}$=0.21
w_{II} =1
W_{IE} =0.15
kinetic parameter
γ **=0.641/1000**

Table S1. Large-scale modeling parameters.

	1	2	3	4	5	6	7	8	9	10	11	12	13	14	15	16	17	18
l-bksts	0	0	0	0	**38**	0	0	0	0	0	0	0	0	**8**	**14**	**1**	0	**21**
l-caAC	0	0	0	0	0	0	0	0	0	0	0	0	0	0	0	0	0	0
l-caMF	**11**	**23**	0	0	**1**	0	0	0	0	0	**5**	0	0	0	0	0	0	0
l-cun	0	0	0	0	0	**2**	0	0	0	0	0	0	0	0	0	0	0	0
l-eR	0	0	0	0	0	0	0	0	0	0	0	0	0	0	0	0	0	0
l-fus	0	0	0	0	0	0	0	0	0	0	0	0	0	0	0	0	0	0
l-infP	0	0	0	0	**11**	0	0	0	0	0	0	0	0	**35**	**51**	**47**	**13**	**23**
l-infT	0	0	0	0	0	0	0	0	0	0	0	0	0	**2**	0	0	0	0
l-iCin	0	0	0	0	0	0	0	0	0	**2**	0	0	0	0	0	0	0	0
l-latOc	0	0	0	0	0	0	0	0	0	0	0	0	0	**1**	**12**	0	0	0
l-latOF	0	0	0	0	0	0	0	0	0	0	0	0	0	0	0	0	0	0
l-lin	0	0	0	0	0	0	0	0	0	**2**	0	0	0	0	0	0	0	0
l-medOF	0	0	0	0	0	0	0	0	0	0	0	0	0	0	0	0	0	0
l-midT	0	0	0	0	0	0	0	0	0	0	0	0	0	**15**	0	0	0	0
l-paraH	0	0	0	0	0	0	0	0	0	**2**	0	0	0	0	0	0	0	0
l-paraCe	0	0	0	0	0	0	0	0	0	0	0	**1**	0	0	0	0	0	0
l-parsOp	0	0	0	0	**8**	0	0	0	0	0	**61**	0	0	0	0	0	**20**	0
l-parsOr	0	0	0	0	0	0	0	0	0	0	0	0	0	0	0	0	0	0
l-parsTr	0	0	0	0	0	0	0	0	0	0	**1**	0	0	0	0	0	**6**	0
l-peric	0	0	0	0	0	0	0	0	0	0	0	0	0	0	0	0	0	0
l-postCe	**1**	**1**	0	0	**6**	0	0	0	0	0	**28**	0	0	0	**3**	0	**19**	**7**
l-postCi	0	0	0	0	0	0	0	0	0	0	0	**18**	0	0	0	0	0	0
l-preCe	**11**	**9**	0	0	**7**	0	0	0	0	0	**39**	0	**1**	0	0	0	9	0
l-precu	0	0	0	0	0	0	0	0	0	0	0	0	0	0	0	0	0	0
l-rAC	0	0	0	0	0	0	0	0	0	0	0	0	0	0	0	0	0	0
l-rMF	0	**4**	0	0	0	0	0	0	0	0	**1**	0	0	0	0	0	0	0
l-supF	0	0	0	0	0	0	0	0	0	0	0	0	0	0	0	0	0	0
l-supP	0	0	0	0	0	0	0	0	0	0	0	0	0	0	**18**	**1**	0	0
l-supT	0	0	0	0	**32**	0	0	0	0	0	**10**	0	0	**4**	**2**	0	**16**	**20**
l-supM	0	0	0	0	**45**	0	0	0	0	0	**3**	0	0	**4**	**32**	**13**	**59**	**57**
l-fronP	0	0	0	0	0	0	0	0	0	0	0	0	0	0	0	0	0	0
l-tempP	0	0	0	0	0	0	0	0	0	0	0	0	0	0	0	0	0	0
l-transT	0	0	0	0	**66**	0	**5**	0	0	0	**16**	0	0	0	0	0	**72**	**74**
l-cCal	0	**5**	0	0	**60**	0	**7**	0	0	0	**15**	0	0	0	0	0	**64**	**33**
r-bksts	0	0	0	0	0	0	0	0	0	0	0	0	0	0	0	0	0	0
r-caAC	0	0	0	0	0	0	0	0	0	0	0	0	0	0	0	0	0	0
r-caMF	0	0	0	0	0	0	0	**14**	0	0	0	0	0	0	0	0	0	0
r-cun	0	0	0	0	0	**30**	0	0	0	0	0	0	0	0	0	0	0	0
r-eR	0	0	0	0	0	0	0	0	0	0	0	0	0	0	0	0	0	0
r-fus	0	0	0	0	0	**22**	0	0	0	0	0	0	0	0	0	0	0	0
r-infP	0	0	0	0	0	**3**	0	0	0	0	0	0	0	0	0	0	0	0
r-infT	0	0	0	0	0	**7**	0	0	0	0	0	0	0	0	0	0	0	0
r-iCin	0	0	0	0	0	**9**	0	0	0	0	0	0	0	0	0	0	0	0
r-latOc	0	0	0	0	0	**37**	0	0	0	0	0	0	0	0	0	0	0	0
r-latOF	0	0	0	0	0	0	0	0	0	0	0	0	0	0	0	0	0	0
r-lin	0	0	0	0	0	**65**	0	0	0	0	0	0	0	0	0	0	0	0
r-medOF	0	0	0	0	0	0	0	0	0	0	0	0	0	0	0	0	0	0
r-midT	0	0	0	0	0	0	0	0	0	0	0	0	0	0	0	0	0	0
r-paraH	0	0	0	0	0	**40**	0	0	0	0	0	0	0	0	0	0	0	0
r-paraCe	0	0	0	0	0	0	0	0	**8**	0	0	0	0	0	0	0	0	0
r-parsOp	0	0	**20**	0	0	0	0	0	0	0	0	0	0	0	0	0	0	0
r-parsOr	0	0	0	0	0	0	0	0	0	0	0	0	0	0	0	0	0	0
r-parsTr	0	0	0	0	0	0	0	0	0	0	0	0	0	0	0	0	0	0
r-peric	0	0	0	0	0	**80**	0	0	0	0	0	0	0	0	0	0	0	0
r-postCe	0	0	**14**	0	0	0	0	**7**	0	0	0	0	0	0	0	0	0	0
r-postCi	0	0	0	0	0	0	0	0	**9**	0	0	0	0	0	0	0	0	0
r-preCe	0	0	**11**	0	0	0	0	**4**	0	0	0	0	0	0	0	0	0	0
r-precu	0	0	0	0	0	**7**	0	0	0	0	0	0	0	0	0	0	0	0
r-rAC	0	0	0	0	0	0	0	0	0	0	0	0	0	0	0	0	0	0
r-rMF	0	0	0	0	0	0	0	0	0	0	0	0	0	0	0	0	0	0
r-supF	0	0	0	0	0	0	0	**3**	0	0	0	0	0	0	0	0	0	0
r-supP	0	0	0	0	0	**1**	0	**16**	0	0	0	0	0	0	0	0	0	0
r-supT	0	0	**14**	0	0	0	0	0	0	0	0	0	0	0	0	0	0	0
r-supM	0	0	**14**	0	0	0	0	0	0	0	0	0	0	0	0	0	0	0
r-fronP	0	0	0	0	0	0	0	0	0	0	0	0	0	0	0	0	0	0
r-tempP	0	0	0	0	0	0	0	0	0	0	0	0	0	0	0	0	0	0
r-transT	0	0	**88**	0	0	0	0	0	0	0	0	0	0	0	0	0	0	0
r-cCal	0	0	**75**	**4**	0	0	0	0	0	0	0	0	0	0	0	0	0	0

Table S2: Lesion percentage in each node (rows) per stroke subject (columns). Lesioned regions are highlighted. Only lesions greater or equal to 1% are shown

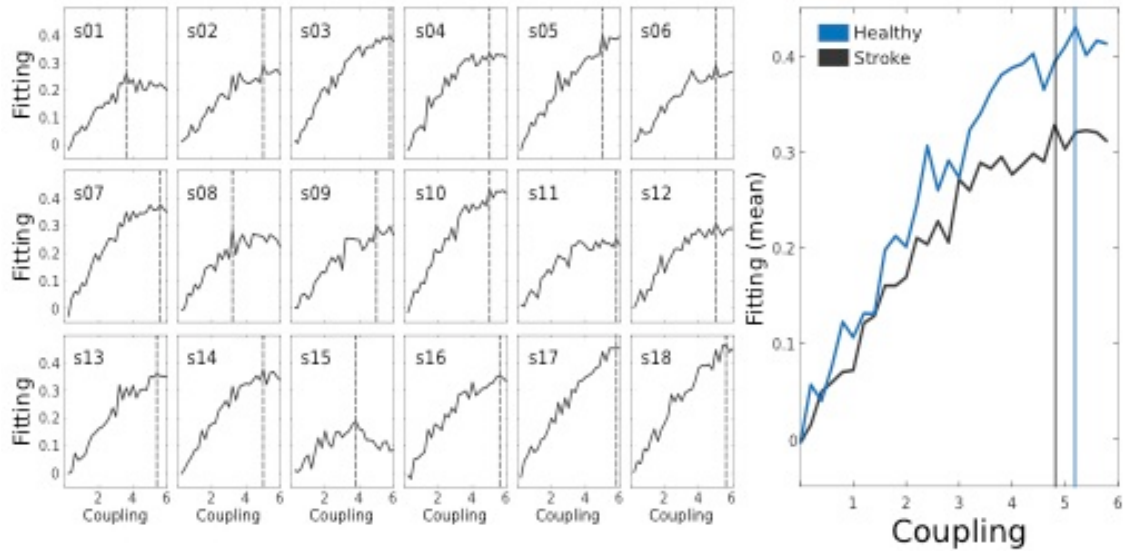

Figure S1: Fitting behavior for all stroke subjects. Subject-specific fitting curves are depicted in the left with optimal fitting marked with a dashed gray line. Mean stroke fitting (dark gray) and healthy fitting (blue) are plotted in the right for comparison.

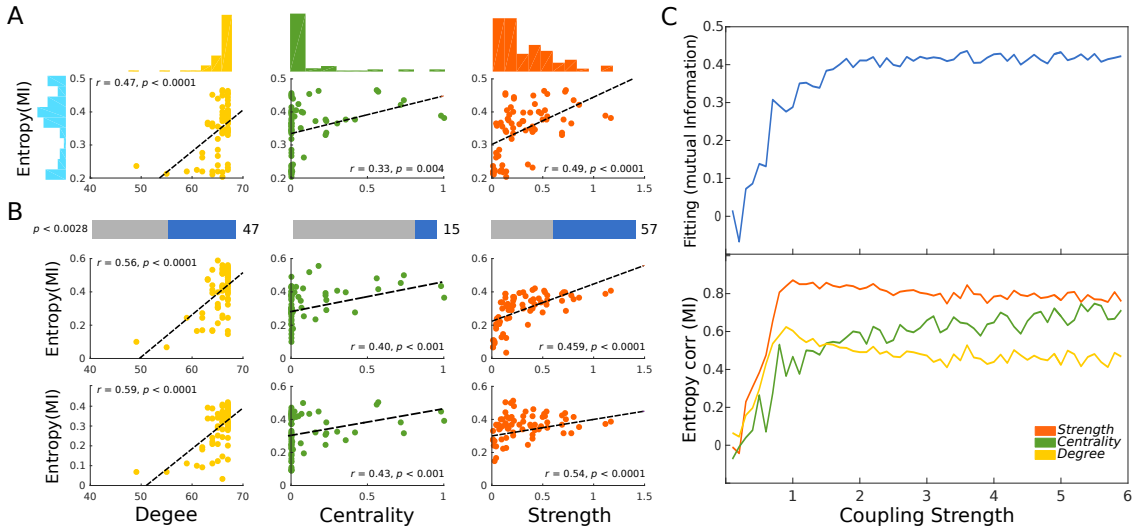

Figure S2: Correlation between node entropy from mutual information FC matrices and three topological metrics in the empirical and modeled data. (A) Scatter plots for correlations in the empirical average healthy control group with their corresponding distributions. (B) Significant subject-by-subject correlations between node entropy and all three metrics. Bars represent the percentage of corrected significant correlations (Bonferroni correction). Scatter plots represent two sample subject-by-subject correlations. (C) Behavior of the fitting and correlations between node entropy and all three topology metrics as a function of the coupling strength. Top plot represents the fitting. Middle plot represents the Pearson correlation between node entropy and degree, centrality and strength.

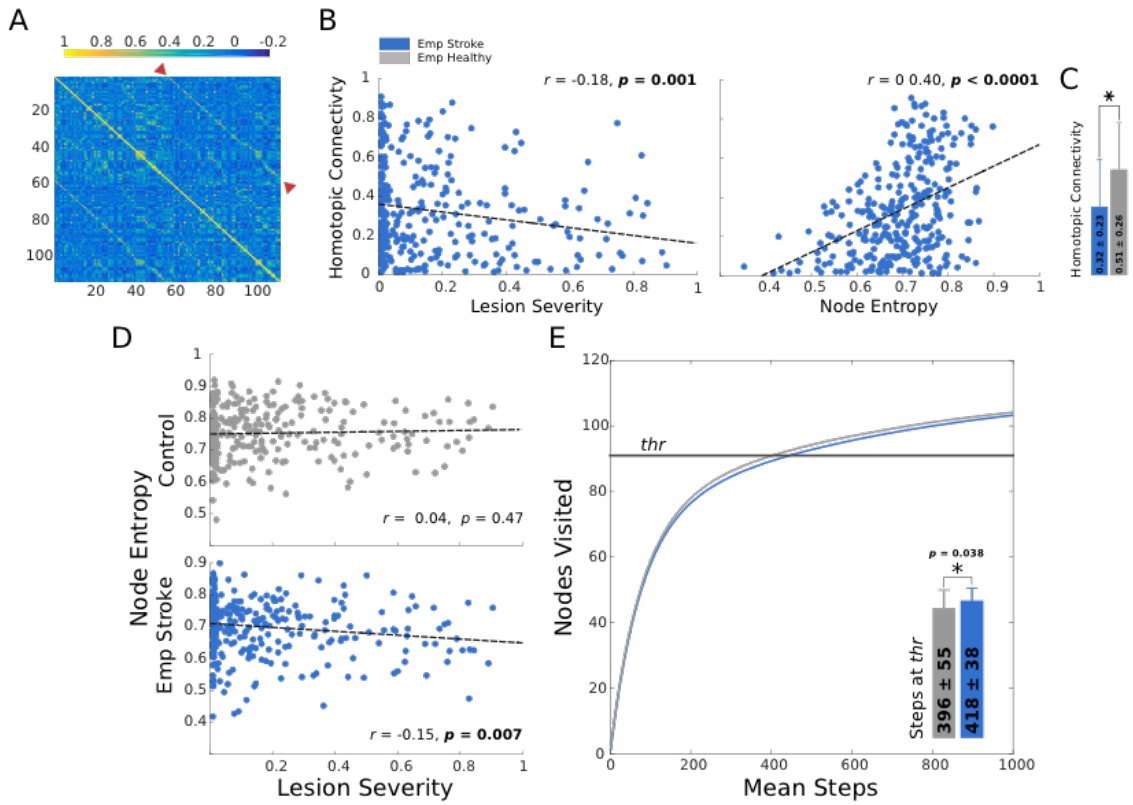

Figure S3: Exploring local and global effects of stroke using a finer parcellation. (A) A sample FC from one stroke patient. Color code indicates correlation values. Homotopic (interhemispheric) connections are highlighted by red arrows. (B) Correlation between lesion severity and homotopic connectivity and node entropy with homotopic connectivity. (C) Mean homotopic connectivity of empirical stroke and healthy patients. The star represents a significant difference ($p < 0.0001$) computed with an unpaired t-test. (D) Correlation between lesion severity and entropy in stroke (blue) and healthy controls. Note that for controls, lesion severity represents the node location index to filter entropy values used as a surrogate control vector. (E) Diffusion of information in the empirical lesioned (blue) and healthy control (grey) brain. Curves represent the mean amount of nodes visited as a function of the walker steps while bars depict the mean steps and standard deviation for each condition. The straight black line represents the threshold (90%) at which steps were counted.

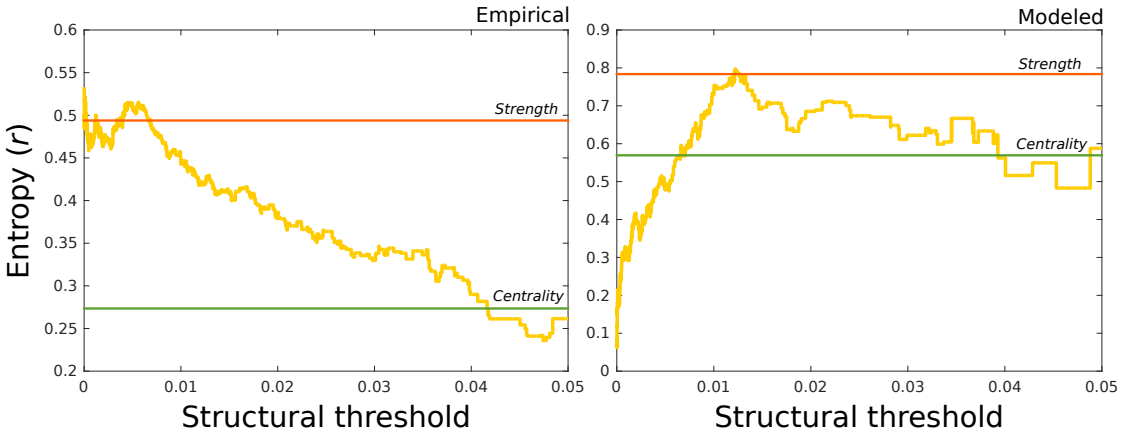

Figure S4: Correlation between degree and node entropy in the empirical and modeled data as a function of the connectivity threshold. Correlation of entropy with strength (red) and centrality (green) are depicted with straight lines for reference.

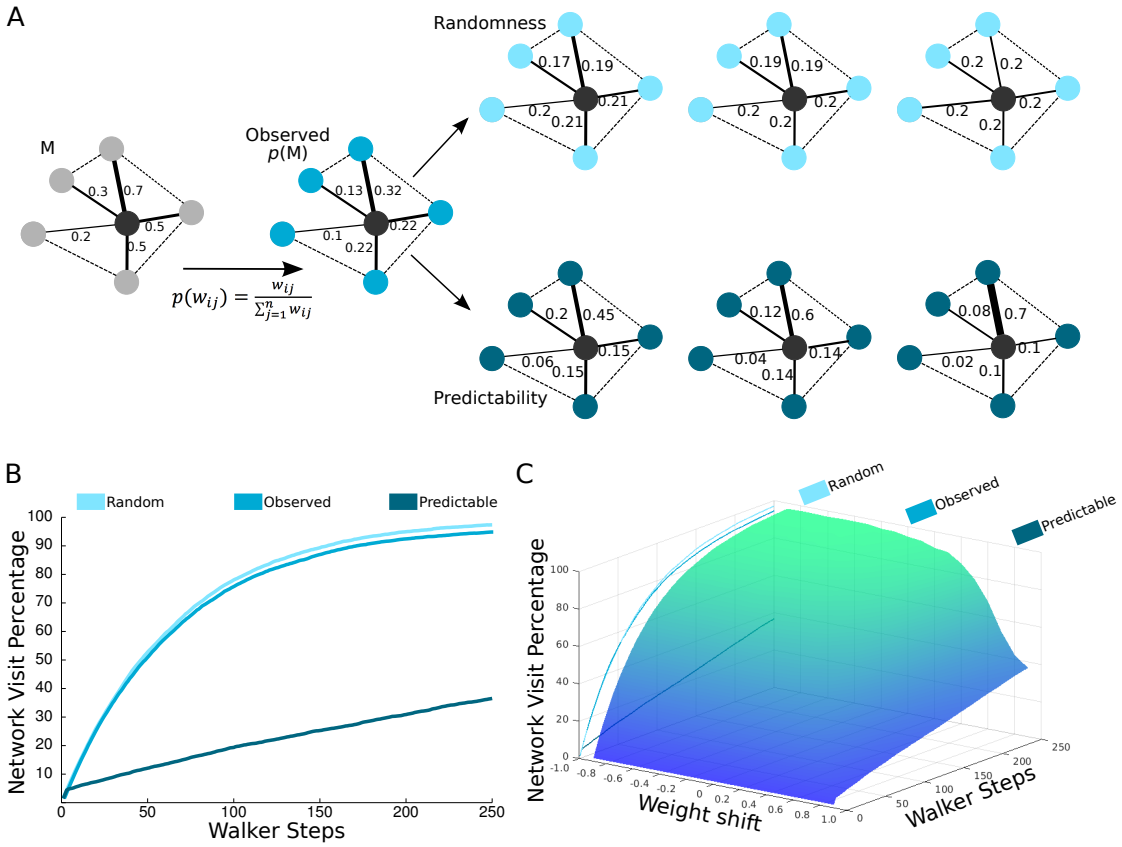

Figure S5: Random-walker simulations in the original and weight-shifted networks. A) Weight-shifting in toy network. The original weights from the functional connectivity matrix M are changed to out-probabilities in order to construct a probability matrix *p*(M). By making these probabilities progressively more similar to each other (top row) the walker diffuses with equal probability (p = 0.2 for all links) while skewing them to just one link (bottom row), the walker is forced to diffuse through the most prominent link with higher probability (p = 0.7). B) Average network visit percentage over 1000 simulations as a function of the walker steps for the original (blue), random-shifted (light-blue) and predictability-shifted (dark-blue) weights. Surface plot representing the landscape of network visit percentage with varying weight shifts. The original network is set at Weight Shift 0. Incrementing randomness to the weight distribution is represented by a negative shift (from 0 to -1), while adding predictability by a positive shift (from 0 to 1). Lighter tones in the surface represent a higher network visit percentage. The boxes in the top depict the weight-shift position of the three walker simulations plotted on the right.